J. Fluid Mech., page 1 of 23. © Cambridge University Press 2011
doi:10.1017/jfm.2011.254

Stability and energy budget of pressure-driven collapsible channel flows

H. F. Liu[1], X. Y. Luo[1]† and Z. X. Cai[2]

[1] Department of Mathematics, University of Glasgow, Glasgow G12 8QW, UK
[2] Department of Mechanics, Tianjin University, 300072, People's Republic of China

(Received 5 July 2010; revised 13 May 2011; accepted 3 June 2011)

Although self-excited oscillations in collapsible channel flows have been extensively studied, our understanding of their origins and mechanisms is still far from complete. In the present paper, we focus on the stability and energy budget of collapsible channel flows using a fluid–beam model with the pressure-driven (inlet pressure specified) condition, and highlight its differences to the flow-driven (i.e. inlet flow specified) system. The numerical finite element scheme used is a spine-based arbitrary Lagrangian–Eulerian method, which is shown to satisfy the geometric conservation law exactly. We find that the stability structure for the pressure-driven system is not a cascade as in the flow-driven case, and the mode-2 instability is no longer the primary onset of the self-excited oscillations. Instead, mode-1 instability becomes the dominating unstable mode. The mode-2 neutral curve is found to be completely enclosed by the mode-1 neutral curve in the pressure drop and wall stiffness space; hence no purely mode-2 unstable solutions exist in the parameter space investigated. By analysing the energy budgets at the neutrally stable points, we can confirm that in the high-wall-tension region (on the upper branch of the mode-1 neutral curve), the stability mechanism is the same as proposed by Jensen & Heil. Namely, self-excited oscillations can grow by extracting kinetic energy from the mean flow, with exactly two-thirds of the net kinetic energy flux dissipated by the oscillations and the remainder balanced by increased dissipation in the mean flow. However, this mechanism cannot explain the energy budget for solutions along the lower branch of the mode-1 neutral curve where greater wall deformation occurs. Nor can it explain the energy budget for the mode-2 neutral oscillations, where the unsteady pressure drop is strongly influenced by the severely collapsed wall, with stronger Bernoulli effects and flow separations. It is clear that more work is required to understand the physical mechanisms operating in different regions of the parameter space, and for different boundary conditions.

Key words: flow–structure interactions, flow–vessel interactions, parametric instability

1. Introduction

Flow in collapsible tubes has aroused considerable interest in the last 20 years due to its potential applications in various biomedical problems. However, recent studies

† Email address for correspondence: xiaoyu.luo@glasgow.ac.uk

are driven more by the rich dynamic behaviour revealed in the Starling resistor type of experiments (Bertram 1982; Bertram, Raymond & Pedley 1990; Bertram & Elliott 2003). Early research focused on simplified 'lumped-parameter' and one-dimensional models (Conrad 1969; Katz, Chen & Moreno 1969; Ishizaka 1972; Shapiro 1977; Kamm & Shapiro 1979; Bertram & Pedley 1982; Cancelli & Pedley 1985; Jensen 1990). This was extended to two-dimensional models in which a segment of upper wall of the flow channel was replaced by an elastic membrane or a thin beam with both extensional and bending forces (Luo & Pedley 1995, 1996, 1998; Pedley & Luo 1998; Luo & Pedley 2000; Jensen & Heil 2003; Stewart *et al.* 2010). Recent progress has been made on three-dimensional models (Hazel & Heil 2003; Marzo, Luo & Bertram 2005; Heil & Waters 2008; Zhu, Luo & Ogden 2008, 2010; Whittaker *et al.* 2010*a*,*b*,*c*,*d*). However, due to the complexity of three-dimensional models and high computational resources, two-dimensional models are still used to understand the mechanisms of the rich dynamic behaviour of the system observed.

Jensen & Heil (2003) analysed a two-dimensional membrane model with the pressure-driven boundary condition (referred to as the pressure-driven system henceforth) for large tension and high Reynolds number, *Re*. They showed that the neutrally stable small-amplitude high-frequency self-excited oscillations in the limit of large membrane tension can grow by extracting kinetic energy from the mean Poiseuille flow faster than it is lost to viscous dissipation, with exactly two-thirds of the net kinetic energy flux dissipated by the (oscillatory) dissipations and the remainder balanced by increased dissipation in the mean flow. Using a fluid–beam two-dimensional model, Luo *et al.* (2008) discovered a 'cascade' stability structure for the flow-driven boundary condition (i.e. in a flow-driven system), and showed that as the wall stiffness is reduced to a critical level, the system loses its stability to various modes of oscillations in a cascade fashion. Interestingly, they found that re-stabilization of an unstable mode is possible below the critical wall stiffness for certain values of Reynolds number. However, the lowest unstable mode in this system was found to be mode-2, whereas only mode-1 instability was identified by Jensen & Heil (2003) for the pressure-driven system in the high-tension and high-*Re* region. (The mode number i, $i = 1, 2, 3\ldots$ here means that the perturbation to the flexible segment contains i half-wavelengths.)

The cascade phenomenon for a flow-driven system was reproduced by Liu *et al.* (2009) using the commercial package ADINA. Liu *et al.* (2009) also confirmed that the occurrence of the lowest unstable mode number is primarily determined by the nature of the inlet boundary conditions; it is mode-1 if the system is pressure-driven, and mode-2 if it is flow-driven. However, they did not show whether the cascade structure still exists if the system is switched from being flow-driven to pressure-driven. Recently, Stewart, Waters & Jensen (2009) analysed the energy budget for high-Reynolds-number and pressure-driven systems, using a one-dimensional analytical model. They showed that the energy budget behaves differently in mode-1 and mode-2 oscillations. For mode-1 oscillations about the uniform base state, the time-averaged net kinetic energy flux into the system is positive, showing that kinetic energy is extracted from the mean flow and is dissipated by the oscillations. However, for mode-2 neutral oscillations, the time-averaged net kinetic energy flux into the system is negative, suggesting a different physical mechanism. This is interesting, although it is not clear if this observation applies to general two-dimensional systems with lower values of tension and Reynolds number (but see discussions in Stewart *et al.* 2010).

The aim of the present study is to address the issues raised above. First, we investigate whether a similar cascade structure exists in the pressure-driven system.

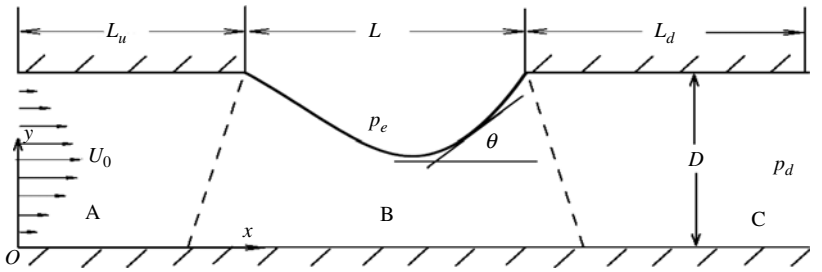

FIGURE 1. The flow–beam configuration (not to scale). Part B has part of the wall replaced by an elastic beam.

We then carry out an energy budget analysis for the neutrally stable modes, and compare our results with those of Stewart *et al.* (2009), in order to assess the energy differences in mode-1 and mode-2 oscillations. Furthermore, we study the differences in the energy budgets between the pressure- and flow-driven systems.

2. Model and method

The model of the collapsible system is composed of flow in a channel in which a part of its rigid upper wall is replaced with an elastic beam in the plane strain configuration (figure 1). The channel has a width of D, a part of the upper wall of length L is replaced by a pre-stressed elastic beam subject to an external pressure of p_e. The upstream and downstream parts of the channel have lengths of L_u and L_d, respectively. The flow is assumed to be incompressible and laminar with the fluid density ρ and viscosity μ and the averaged velocity of U_0. The extensional and bending stiffnesses of the beam are denoted as EA and EI, respectively, where E is Young's modulus applicable for plain strain problems, A is the cross-sectional area of the beam (given that the beam has unit width in the z-direction, A is effectively the beam's thickness h), and I is the second moment of area of the beam cross-section. The mass, damping and rotational inertia of the beam are neglected.

2.1. *The fluid–beam model*

2.1.1. *Governing equations*

For convenience, all variables are non-dimensionalised as follows:

$$\left.\begin{aligned} &u_i = \frac{u_i^*}{U_0}, \quad \sigma_{ij} = \frac{\sigma_{ij}^*}{\rho U_0^2}, \quad p_i = \frac{p_i^*}{\rho U_0^2}, \quad t = \frac{t^* U_0}{D}, \quad l = \frac{l^*}{D}, \quad x = \frac{x^*}{D}, \\ &y = \frac{y^*}{D} \quad (i, j = 1, 2), \end{aligned}\right\} \tag{2.1a}$$

where non-dimensional flow velocity components are denoted by u_i, fluid stresses σ_{ij}, pressure p, time t, length l, Cartesian coordinates x, y, and dimensional quantities are denoted with a star.

The non-dimensional parameters are defined as

$$T = \frac{T^*}{\rho U_0^2 D}, \quad c_\lambda = \frac{EA}{\rho U_0^2 D}, \quad c_\kappa = \frac{EI}{\rho U_0^2 D^3}, \quad Re = \frac{U_0 D \rho}{\mu} \tag{2.1b}$$

where T is the tension of the beam, c_λ is the extensional stiffness, c_κ is the flexural rigidity, and Re is the Reynolds number.

The governing equations for the fluid flow are the Navier–Stokes equations

$$\frac{\partial u_i}{\partial t} + u_j u_{i,j} = \sigma_{ij,j}, \tag{2.2}$$

$$u_{i,i} = 0, \quad i, j = 1, 2, \tag{2.3}$$

where $\sigma_{ij} = -p\delta_{ij} + (1/Re)u_{i,j}$. Here δ_{ij} is the Kronecker delta. By employing the Kirchhoff constitutive laws for the (massless) elastic beam, we can write the following dimensionless governing equations for the beam (for derivation of these equations, see Cai & Luo 2003):

$$c_\kappa \kappa \kappa' + c_\lambda \lambda' + \lambda \tau_n = 0, \tag{2.4}$$

$$c_\kappa \left(\frac{1}{\lambda}\kappa'\right)' - \lambda \kappa T - c_\lambda \lambda \kappa (\lambda - 1) = \lambda (\sigma_n - p_e), \tag{2.5}$$

$$x' = \lambda \cos\theta, \quad y' = \lambda \sin\theta, \quad \theta' = \lambda\kappa, \tag{2.6}$$

where κ is the non-dimensional curvature ($\kappa = \kappa^* D$), the superscript prime stands for a derivative with respect to the initial beam position l, the arc-length of the beam is denoted as s ($s = \lambda l, 0 < s < s_0$), and λ is the principal stretch of the beam, defined as

$$\lambda = \sqrt{x'^2 + y'^2}. \tag{2.7}$$

In (2.4)–(2.6), θ stands for the rotation angle of the beam from the x-axis; σ_n, τ_n are fluid stresses applied on the beam in the normal and tangential directions, (n, s), respectively:

$$\sigma_n = p - \frac{2}{Re}\frac{\partial u_n}{\partial n}, \quad \tau_n = -\frac{1}{Re}\left(\frac{\partial u_s}{\partial n} + \frac{\partial u_n}{\partial s}\right). \tag{2.8}$$

2.1.2. *Boundary conditions*

The boundary conditions are set up in the following fashion: at the outlet, a stress free condition is used ($p_d \approx 0$); along the walls, a no-slip boundary condition is applied, and at the two ends of the beam, a clamped support is employed.

In addition, for a pressure-driven system, a constant upstream pressure is imposed, whereas for the flow-driven system a parabolic velocity profile is specified at the upstream inlet.

2.2. *Numerical schemes*

Two approaches are used to solve the fluid–beam model. One is the fully coupled fluid–structure interaction (FSI) solver for the unsteady flows, and the other is the eigenvalue solver for the linear stability analysis. These are described in detail in Cai & Luo (2003) and Luo *et al.* (2008) but will be briefly mentioned here for completeness.

Fully coupled FSI solver

The fully coupled unsteady nonlinear FSI equations are discretized using the spine method, in which the moving grids are parameterized with the positions of a set of spines. One end of these spines is fixed at the lower boundary of the channel, and the other end is attached to the material point on the elastic beam (Cai & Luo 2003). The Petrov–Galerkin weighted residual method is then used in the finite element approach. The method can be categorized as an arbitrary Lagrangian–Eulerian (ALE) finite element formulation. The fluid grid uses triangular 6-node elements with a second-order shape function for u, v and a linear function for p, while the solid grid uses 3-node beam elements with a second-order shape function for $x, y, \theta, \lambda, \kappa$. The

discretized finite element matrix equation is

$$\boldsymbol{M}(\boldsymbol{U})\frac{\mathrm{d}\boldsymbol{U}}{\mathrm{d}t} + \boldsymbol{K}(\boldsymbol{U})\boldsymbol{U} - \boldsymbol{F} = \boldsymbol{R} = 0, \tag{2.9}$$

where $\boldsymbol{U} = (u_j, v_j, p_j, x_j, y_j, \theta_j, \lambda_j, \kappa_j)$ is the global vector of unknowns, with $j = 1, 2, \ldots n$ denoting the nodal number, $\boldsymbol{R}$ is the overall residual vector, and $\boldsymbol{F}$ is the external force vector. Equation (2.9) is solved with an implicit finite difference second-order predictor–corrector scheme with variable time steps (Cai & Luo 2003). Note that in general ALE methods may fail to satisfy the geometric conservation law, which tends to lose the order of temporal convergence on a moving grid (Étienne, Garon & Pelletier 2009). However, we can prove that this problem disappears completely in the particular spine-based ALE approach used (see Appendix). As the result, the accuracy of the numerical scheme used (second-order) is not compromised due to the moving grid. However, in practice, due to a possible restart in the course of time, and the irregular boundary conditions, the effective order of temporal convergence could drop slightly below two. This occurs for simulations of fixed grids too.

The eigenvalue solver

The linear stability is studied by applying an infinitesimal perturbation, $\Delta\boldsymbol{U} = \mathrm{e}^{\omega t}\tilde{\boldsymbol{U}}$, to the nonlinear steady solution $\bar{\boldsymbol{U}}$, where $\omega(=\omega_r + \mathrm{i}\omega_i)$ and $\tilde{\boldsymbol{U}}$ are the complex eigenvalue and eigenvector, respectively. Upon substituting the perturbed solution into (2.9), and dropping the higher-order terms, we derive the eigenvalue equation in the form

$$(\omega\bar{\boldsymbol{M}} + \bar{\boldsymbol{K}})\tilde{\boldsymbol{U}} = 0, \tag{2.10}$$

where the matrices $\bar{\boldsymbol{M}}, \bar{\boldsymbol{K}}$ are functions of $\bar{\boldsymbol{U}}$. Equation (2.10) is solved with a QZ algorithm for the complete set of eigensolutions of the system, which can be extremely laborious (Garbow 1978). Note that the definition of the eigenvalue problem used here means that the imaginary part of the eigenvalue indicates the frequency, and the real part denotes the growth. This is different to the conventional notation.

To locate a neutral point (corresponding to $\omega_r = 0$), we scan the parameter space in question by sweeping in the x-direction and bisecting in the y-direction. Due to the expensive nature in terms of RAM of the QZ solver, a grid with the maximum 2944 nodes is employed for the eigensolver. However, all results of the eigensolver are further checked with the full unsteady solver on a much refined grid of 22 000 nodes, to ensure the reliability of the eigensolver. Computation time is ∼0.1–1 CPU min for each single time step. However, typical time for locating a neutral point can take from a few hours to 2–3 days (including manual adjustments and bisections).

2.3. *The energy budget analysis*

The energy budget of the system can be derived from the momentum equation of the fluid (2.2). Multiplying both sides of (2.2) with velocity u_i and integrating over the whole domain, Ω, we have

$$\int_\Omega u_i\frac{\partial u_i}{\partial t}\,\mathrm{d}\Omega + \int_\Omega u_i u_{i,j} u_j\,\mathrm{d}\Omega = \int_\Omega u_i\sigma_{ij,j}\,\mathrm{d}\Omega. \tag{2.11}$$

This leads to

$$\frac{1}{2}\int_\Omega\left(\frac{\partial q^2}{\partial t}\right)\mathrm{d}\Omega + \frac{1}{2}\int_\Gamma q^2 u_j n_j\,\mathrm{d}\Gamma = \int_\Gamma \sigma_{ij}n_j u_i\,\mathrm{d}\Gamma - \int_\Omega \sigma_{ij}u_{i,j}\,\mathrm{d}\Omega, \tag{2.12}$$

where $q^2 = \sum u_i u_i$, and Γ denotes the boundary of the domain.

$P_1, \bar{P}_1$	The rate of work of upstream pressure
$\mathrm{d}E, \mathrm{d}\bar{E}$	The rate of change of kinetic energy, as defined in (2.17)
$F, \bar{F}$	The rate of net kinetic energy flux into the system
$D, \bar{D}$	The rate of viscous dissipation
$\bar{D}_s$	The rate of viscous dissipation due to oscillatory motion
$\bar{D}_p$	The rate of viscous dissipation due to steady motion
$P_2, \bar{P}_2$	The rate of change of energy stored in the beam
$\mathrm{d}U_\lambda, \mathrm{d}\bar{U}_\lambda$	The rate of stretching strain energy in the beam
$\mathrm{d}U_\kappa, \mathrm{d}\bar{U}_\kappa$	The rate of bending strain energy in the beam
$P_3, \bar{P}_3$	The rate of work done by the external pressure to the beam

TABLE 1. Definition of the energy budgets; the overbar indicates the averaged quantity of a neutral cycle.

Using the notations introduced in table 1, (2.12) can be expressed as

$$P = \mathrm{d}E - F + D, \tag{2.13}$$

where

$$\begin{aligned} F &= -\frac{1}{2}\int_\Gamma q^2 u_j n_j \,\mathrm{d}\Gamma \\ &= \frac{1}{2}\int_0^1 q^2 u\Big|_{inlet}\,\mathrm{d}y - \frac{1}{2}\int_0^1 q^2 u\Big|_{outlet}\,\mathrm{d}y - \frac{1}{2}\int_0^{S_0} q^2 u_n \,\mathrm{d}s, \end{aligned} \tag{2.14}$$

$$P = \int_\Gamma \sigma_{ij} n_j u_i \,\mathrm{d}\Gamma = \int_0^1 p_u u \,\mathrm{d}y - \int_0^{S_0} (\tau_n u_s + \sigma_n u_n)\,\mathrm{d}s = P_1 - P_2, \tag{2.15}$$

with

$$P_1 = \int_0^1 p_u u \,\mathrm{d}y, \quad P_2 = \int_0^{S_0} (\tau_n u_s + \sigma_n u_n)\,\mathrm{d}s. \tag{2.16}$$

Special attention should be paid to the computation of $\mathrm{d}E$ using the ALE formulation, since

$$\mathrm{d}E = \frac{1}{2}\int_\Omega \left(\frac{\partial q^2}{\partial t}\right)\mathrm{d}\Omega = \frac{1}{2}\int_\Omega \left(\frac{\delta q^2}{\delta t} - \dot{x}_j q_{,j}^2\right)\mathrm{d}\Omega, \tag{2.17}$$

where $\delta/\delta t$ is the time derivative following a moving node of velocity $\dot{x}_j$, which is different to $\partial/\partial t$ used in (2.12), in the Eulerian frame of reference.

We can further associate P_2 with the rate of energy stored in the beam. Substituting (2.4) and (2.5) into (2.16), we have

$$P_2 = (P_3 + \mathrm{d}U_\lambda + \mathrm{d}U_\kappa), \tag{2.18}$$

$$P_3 = \int_0^{s_0} p_e u_n \,\mathrm{d}s, \tag{2.19a}$$

$$\mathrm{d}U_\lambda = \int_0^L \left[c_\lambda(\lambda - 1)\frac{\partial \lambda}{\partial t} - \lambda\kappa T u_n\right]\mathrm{d}l, \tag{2.19b}$$

$$\mathrm{d}U_\kappa = \int_0^L c_\kappa \kappa \frac{\partial(\kappa\lambda)}{\partial t}\,\mathrm{d}l. \tag{2.19c}$$

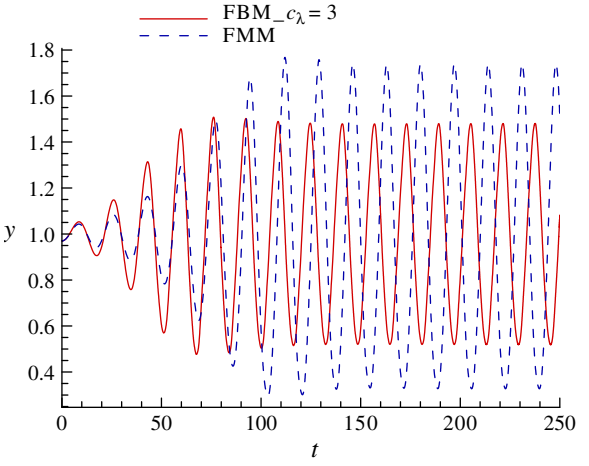

FIGURE 2. (Colour online available at journals.cambridge.org/flm) Wall displacement $y(t)$ at $x(t = 0) = 7.5$ for the test case, where the solid curve indicates the fluid–beam model and the dashed one denotes the fluid–membrane model.

Therefore, the rate of work done by all forces for the system can be written as

$$P_1 = \mathrm{d}E - F + D + P_3 + \mathrm{d}U_\lambda + \mathrm{d}U_\kappa. \tag{2.20}$$

Equation (2.20) states that the rate of work done by the upstream pressure (P_1) is balanced by the rate of change of: the kinetic energy ($\mathrm{d}E$), net kinetic energy flux into the system (F), viscous dissipation (D), work done by the beam to overcome the external pressure (P_3), and strain energies inside the beam ($\mathrm{d}U_\lambda, \mathrm{d}U_\kappa$).

3. Results

3.1. *Validation*

The numerical code has been tested extensively for the flow-driven system (Cai & Luo 2003; Luo *et al.* 2008). Here we will focus on validation of the pressure-driven system, which has thinner boundary layers near the upstream entrance, especially for higher tension and Reynolds numbers. Extensive grid independence and temporal accuracy tests were carried out before choosing the final grid of 23 000 nodes and the residual tolerance of 10^{-6}.

The validation case is chosen to have: $D = 1$, $L_u = 5$, $L = 10$, $L_d = 30$, and $Re = 450$, $T = 100$, $p_e = 0.966\,77$, following Jensen & Heil (2003) see figure 2. In order to compare our results with Jensen & Heil (2003)'s analysis, which is applicable for a membrane with a constant longitudinal tension, we use two different elastic models here: the fluid–beam and the fluid–membrane models. For validation purposes, we choose the wall stiffness c_λ to be small in the fluid–beam model to reduce the effects of deformation-induced tension and bending. Grid independence tests indicate that in order to capture the effects of the thin Stokes layer for this case, a non-uniform grid with over 23 000 nodes is required for both models. This is much finer than the grids used for the flow-driven system (Cai & Luo 2003).

The steady equilibrium state is achieved in the same manner as Jensen & Heil (2003): with the non-dimensional inlet pressure adjusted to an initial position where the mid-point of the elastic section is in alignment with the upper rigid channel wall (initial position) and the rest bulges out upstream and deflects inward downstream. The

initial condition, to which the perturbation is applied, is reached when the external pressure is such that the mid-point displacement is lowered to within -0.03 of the undeformed configuration.

The steady results obtained with the fluid–beam, and the fluid–membrane models are almost identical to those of Jensen & Heil (2003) for the two cases tested. The unsteady results, however, are slightly different between the beam and membrane models. Figure 2 shows the unsteady wall history plotted at the centre of the elastic wall. The fluid–membrane model agrees quite well with that of Jensen & Heil (2003): the amplitude of y ($x = 10$) varies between 0.331 and 1.77, and the frequency is $\sim$0.06. In other words, the difference in amplitude is within 5 % of the peak deflection (Jensen & Heil 2003) (their figure 10), and the difference in frequency is virtually zero. The amplitude predicted by the fluid–beam model is slightly smaller, although the frequency is similar ($\sim$0.06). This is because the fluid–beam model has bending and stretch-induced tension; although we set these to be small, they are significant through the two clamped ends. As reported by Liu *et al.* (2009), small differences in model assumptions could lead to noticeable differences in the unsteady behaviour. We should bear this in mind when comparing the stability of the fluid–beam model with the membrane model used by Jensen & Heil (2003). Indeed, good quantitative agreement is obtained if we also use the fluid–membrane model. In addition, we can reproduce the neutral stability curve, including the turning point, of the group's more recent work (Stewart *et al.* 2010), where they used the method of matched eigenfunction expansions and plotted the critical Reynolds number versus tension in the pressure-driven system (see figure 3 therein).

In §§ 3.2–3.3 below, we investigate the stability of the system using the eigensolver.

3.2. *The stability structure in the c_λ–Re space*

To investigate changes of the stability structure in the pressure-driven system, in the following, we will use the channel geometry with $D = 1$, $L_u = 5$, $L = 5$ and $L_d = 30$, $p_e = 1.95$ and $T = 0$, as in Luo *et al.* (2008).

As stated earlier, locating a neutral point in the c_λ–Re space using the QZ solver is extremely time-consuming. Simulating flow in the pressure-driven system poses additional challenges; we need to use much refined grids to resolve the thin boundary layers at the upstream end, and to adjust the driving pressure manually so that the Reynolds number (which is computed) remains unchanged in the (c_λ, Re) space. For this reason, here we will compute the change of the stability structure for $Re = 300$ only.

The neutral points of the pressure-driven system are shown in table 2. In particular, the mode-2 neutral curve has an upper branch (from stable to unstable as c_λ is reduced), and a lower branch (from unstable to stable as c_λ is reduced). One could speculate that there exist similar upper and lower branches in the mode-1 neutral curve; if so we should locate two mode-1 points with Re fixed at 300. Indeed, we have found the mode-1 neutral point on the upper branch, albeit at a very large value of c_λ ($\sim 10^8$). However, on the 'lower branch', the oscillatory mode-1 becomes static divergent, i.e. the oscillatory frequency approaches zero as the growth rate vanishes. In other words, we see a mode switch at the lower branch.

It is possible that a more complete mode-1 curve (i.e. with a proper lower branch) exists elsewhere in the (c_λ, Re) space but we only looked at $Re = 300$ (see § 3.3 below).

Pressure driven:	Lower neutral branch	Upper neutral branch
Mode-1 unstable zone	$c_\lambda \geqslant 105$ $(\omega_i = 0)$ static divergence point	$c_\lambda \leqslant 10^8$ $(\omega_i = 6.33)$
Mode-2 unstable zone	$c_\lambda \geqslant 241.1 (\omega_i = 1.18)$	$c_\lambda \leqslant 2465$ $(\omega_i = 2.38)$
Mode-3 unstable zone		$c_\lambda \leqslant 329.2$ $(\omega_i = 4.20)$
Flow-driven (Luo *et al.* 2008):		
Mode-2 unstable zone	$c_\lambda \geqslant 475.4$ $(\omega_i = 1.3)$	$c_\lambda \leqslant 1756.3$ $(\omega_i = 1.98)$
Mode-3 unstable zone		$c_\lambda \leqslant 323.2$ $(\omega_i = 4.93)$

TABLE 2. Unstable zones of the pressure driven system at $Re = 300$, and $p_e = 1.95$. The limits of the unstable zones are indicated by the neutral points. The comparison with the flow-driven system by Luo *et al.* (2008) will be mentioned in the discussion.

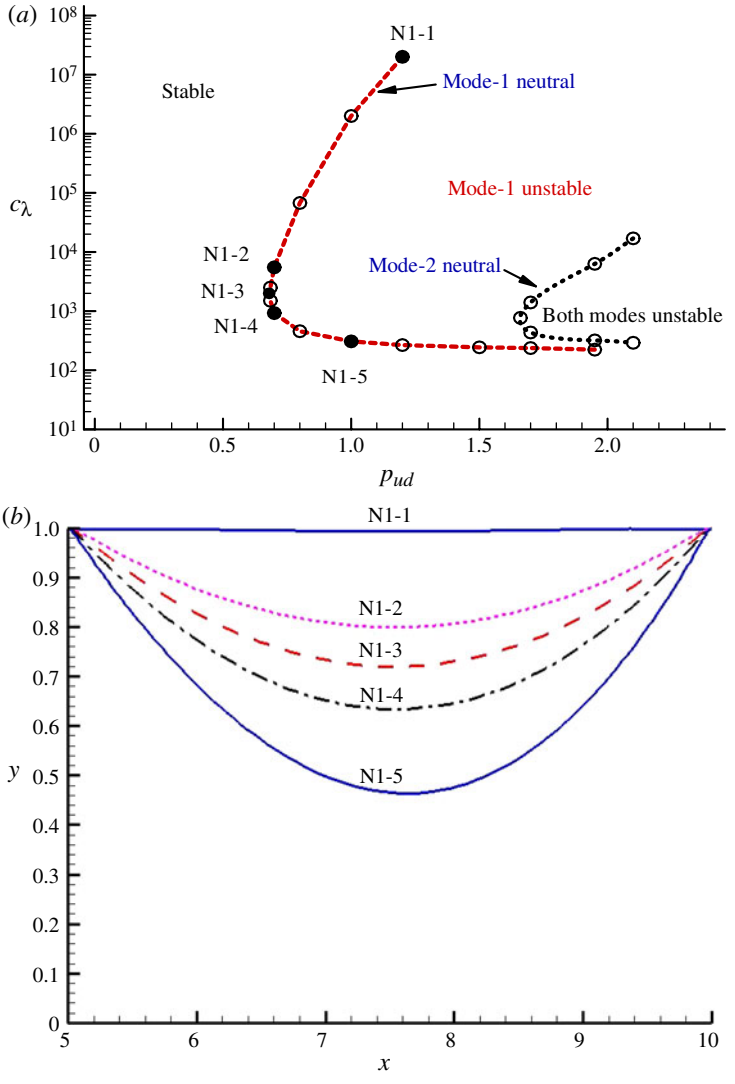

FIGURE 3. (Colour online) (*a*) The mode-1 and mode-2 neutral curves of the pressure-driven system in the (p_{ud}, c_λ) space. The (dimensional) external transmural pressure is kept constant at 1.755 Pa. The computed *Re* values are between 104.4 and 219. The lowest *Re* value occurred at a position between N1-4 and N1-5, and the highest value is at N1-1 (see table 2 for more information). (*b*) The corresponding steady elastic wall shapes at selected mode-1 neutral operating points (filled circles in (*a*)).

3.3. *The stability structure in the* (p_{ud}, c_λ) *space*

Since the driving pressure is the control parameter, it is much easier to identify the stability structure in the (p_{ud}, c_λ) space. Note that unlike Luo *et al.* (2008) where the non-dimensional external pressure value is kept constant ($p_e = 1.95$), here the dimensional external pressure is kept constant (i.e. $p_e^* = 1.755$ Pa, which corresponds to $p_e = 1.95$ at $Re = 300$), since we can no longer use *Re* to non-dimensionalise the pressure.

Figure 3(*a*) shows the stability structure of the pressure-driven system in the (p_{ud}, c_λ) space. Here, we have a more complete mode-1 neutral curve. The mode-2 curve seems to be wrapped inside the mode-1 neutral curve for the range of parameters investigated. This is very different to the cascade structure found in the flow-driven system, and suggests that the dominant unstable mode is mode-1 for the pressure-driven system. The flow-driven system reported by Luo *et al.* (2008) is primarily unstable to mode-2 perturbations. Clearly, the underlying mechanisms for these two systems are different. In the following, we explore the system further using an energy budget analysis based on the full unsteady solver.

3.4. *Energy budget analysis*

The full unsteady numerical solver is used to compute the energy budget during the neutral oscillations. The energy budget for a selection of points along the mode-1 neutral curve was computed; the corresponding steady wall shapes for these points are shown in figure 3(*b*). To compare the results with those of Stewart *et al.* (2009), we estimated the following quantities from the energy budgets of the neutral points. When averaged over a oscillating period, (2.20) reduces to

$$\bar{F} + \bar{P}_1 = \bar{D} = \bar{D}_p + \bar{D}_s, \tag{3.1}$$

where $\bar{D}_p$ is the viscous dissipation due to the mean flow, and $\bar{D}_s$ is the oscillatory dissipation. The dissipation of energy in mean flow can be obtained by calculating the energy dissipation with the time-averaged velocity vector $\bar{u}_i$ and the time-averaged position vector $\bar{x}_i$ over one period. $\bar{D}_s$ is then be obtained by simply subtracting $\bar{D}_p$ from $\bar{D}$.

For convenience, the energy budget definitions are summarized in table 1. The averaged values are estimated numerically during the post-processing, and are listed in table 3, together with the averaged rate of change of kinetic energy and the neutral frequency. Note that at the exact location of the neutral points, $\mathrm{d}\bar{E} \equiv 0$. However, as we used a numerical scheme to estimate the neutral position, as well as the energy budget terms, the values of $\mathrm{d}\bar{E}$ are only approximately zero. Therefore when $\mathrm{d}\bar{E}$ is sufficiently small (i.e. it is at least an order of magnitude smaller than other energy budget terms at the same point), the averaged quantities computed are reliable; otherwise these are only qualitatively indicative.

Table 3 shows that $\bar{F}$ is positive for all the mode-1 neutral points selected (it is definitely positive for N1-1, N1-2 and N1-3, but too small to be judged for N1-4 and N1-5), i.e. the influx upstream provides energy into the system to maintain the oscillation.

Table 3 shows that the ratio $\bar{D}_s/\bar{F}$ is 0.711 for N1-1 on the upper branch of the mode-1 neutral curve. The $\bar{D}_s/\bar{F}$ ratio is predicted to be 2/3 in an asymptotic predication for large-membrane tension by Jensen & Heil (2003), which states that for the almost undeformed configuration, the self-excited mode-1 oscillations grow by extracting kinetic energy, with exactly two-thirds of the net kinetic energy flux dissipated by the oscillations, and the remainder balanced by increased dissipation in the mean flow. Table 3 seems to suggest that oscillations of N1-1 may be controlled by the same mechanism. The small numerical discrepancy (∼6 %) between the estimated values and 2/3 may be attributed to numerical errors, such as the problem of locating the neutral position exactly and the numerical error in estimating the energy quantities.

However, as we follow the mode-1 neutral curve downwards, the wall deformation increases as wall stiffness decreases, and the whole energy balance changes; $\bar{D}_s$

Point	$\bar{F}$	$\bar{P}_1$	$\bar{D}$	$\bar{D}_s$	$\bar{D}_s/\bar{F}$	$\mathrm{d}\bar{E}$	ω_i	Re
N1-1	1.118×10^{-3}	8.995×10^{-1}	9.002×10^{-1}	7.951×10^{-4}	0.711	8.117×10^{-6}	3.623	219.00
N1-2	7.050×10^{-5}	2.845×10^{-1}	2.846×10^{-1}	6.174×10^{-5}	0.875	-7.634×10^{-7}	1.016	121.90
N1-3	1.820×10^{-5}	2.554×10^{-1}	2.555×10^{-1}	1.898×10^{-4}	10.420	-1.136×10^{-4}	0.848	112.66
N1-4	7.838×10^{-5}	2.505×10^{-1}	2.509×10^{-1}	3.936×10^{-4}		-2.148×10^{-4}	0.726	107.40
N1-5	3.619×10^{-4}	3.834×10^{-1}	3.845×10^{-1}	5.353×10^{-3}		-6.303×10^{-4}	0.519	115.60

TABLE 3. List of the time-averaged quantities at selected operating points. Note that the computed *Re* values reflect the pressure drop, but are not exactly proportional to it as the wall deformation is different at these points.

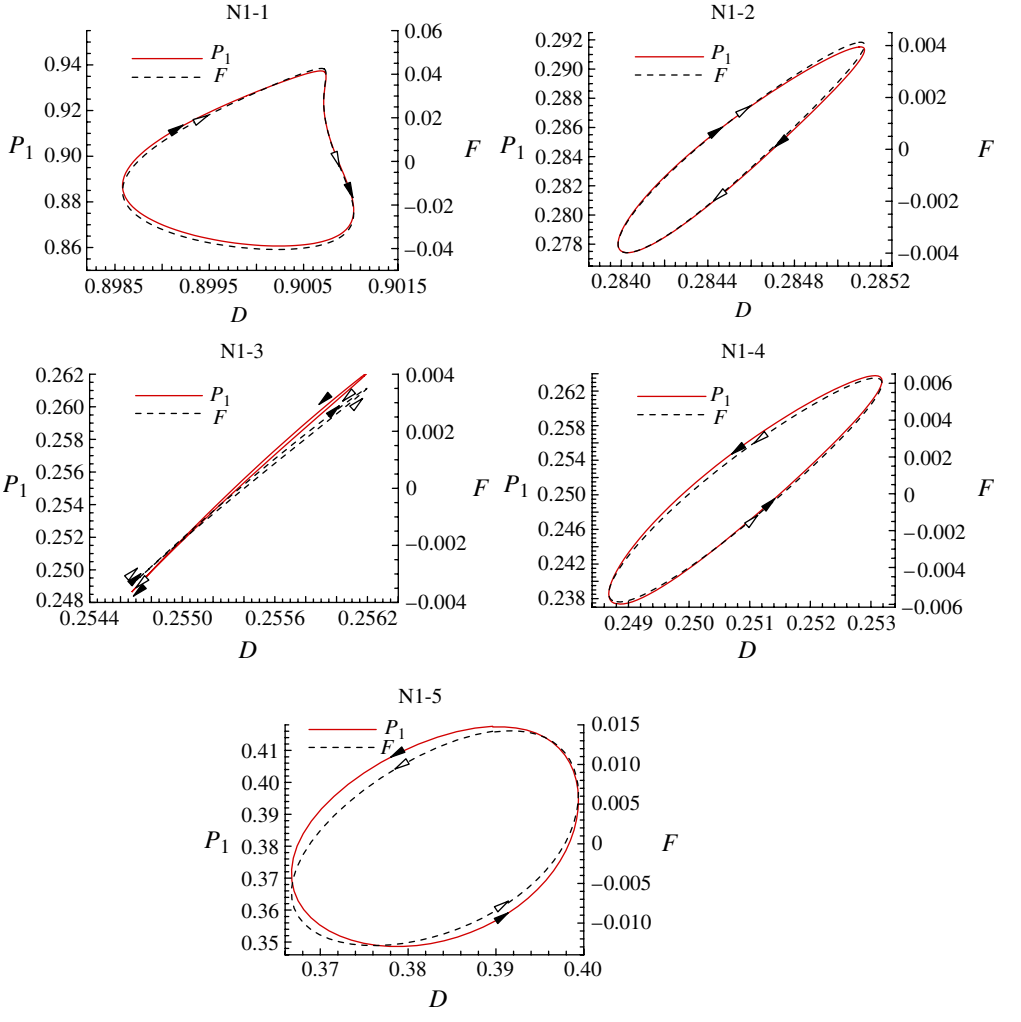

FIGURE 4. (Colour online) Phase plots of the mode-1 F and P_1 against D of the pressure-driven system.

becomes relatively larger than $\bar{F}$ and the ratio $\bar{D}_s/\bar{F}$ exceeds 5 as we pass the turning point, N1-3 (table 3).

On the lower branch, $\bar{D}_s$ is an order of magnitude greater than $\bar{F}$. This means that the sloshing motion along the channel no longer dominates and the influx alone is insufficient to sustain the transversal motion of the mode-1 oscillation. Instead, the driving pressure is doing more work to overcome the increased viscous dissipation due to a more collapsed channel wall. In other words, the mechanism predicted by the asymptotic analysis is no longer valid for the lower branch of the mode-1 neutral curve. This agrees with the recent work by Stewart *et al.* (2010).

Plots of F and P_1 against D over one period along with their temporal evolutions for the operating points are shown in figures 4 and 5. Since F and P_1 are almost in phase, in the following, we will focus on the phase difference between F and D only.

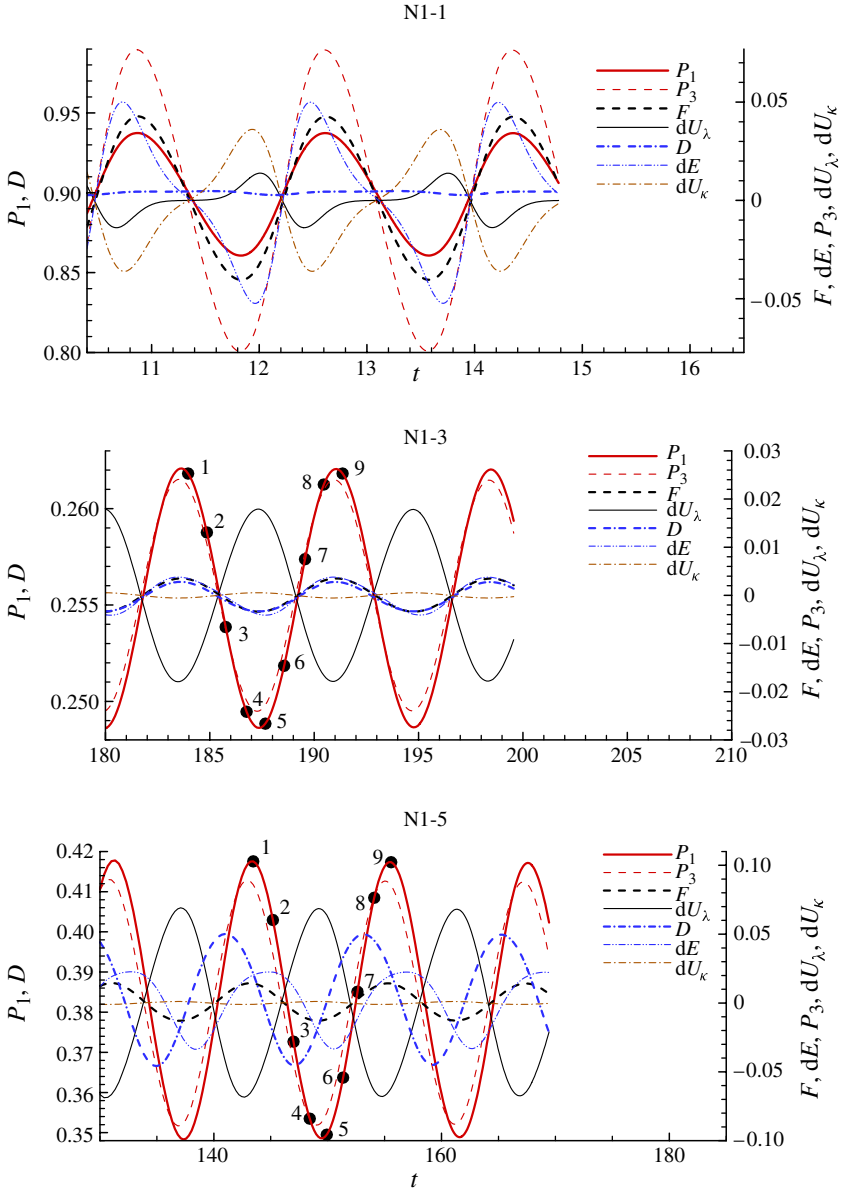

FIGURE 5. (Colour online) Variation of the energy budgets in time of selected mode-1 neutral points.

Remarkably, the phase diagrams of the points along the upper branch (figure 4) qualitatively resemble the phase plots by Stewart *et al.* (2009 figure 11). The loops are in a clockwise direction. However, Stewart *et al.* (2009) also observed a longer and rounder trough of F which leads to a long narrow anticlockwise region below the large loop, which is absent here. This may be due to the one-dimensional approximations introduced by Stewart *et al.* but it is also possible that the upper branch control parameters (tension and Re) used here are still lower than in their parameter region. It is interesting to see that for N1-1, there are two local minima of D over one period,

and the global minimum of D occurs when F is close to zero. This suggests that the rate of net kinetic energy influx drives the oscillation, which in turn increases the rate of viscous dissipation.

The solutions on the lower branch of the mode-1 curve show a different picture: the F–D relation is now anticlockwise. This is confirmed by the corresponding temporal evolution of F and D on the right; the anti/clockwise F–D relation indicates a phase lag/lead between F and D. The change of the phase direction occurs at the turning point; and the phase plot collapses to a very narrow figure-eight shape, with an anticlockwise direction on the top and clockwise on the bottom. In other words, F and D are almost in phase. The observation that F and D are in phase at the turning point is of physical significance for separating the mechanisms responsible for the system behaviour in the high-tension and high-Re region from those of the lower-tension and lower-Re region.

We also observe that as the wall stiffness is reduced (for a fixed p_{ud}), the system first becomes unstable to a mode-1 perturbation when the net rate of kinetic energy influx F leads the rate of dissipation D, while a further reduction of c_λ stabilized mode-1, and D leads F in phase. The further along the curve the solution is from the turning point, the greater the phase difference between F and D. Note that the global minimum of D still seems to correlate with $F \approx 0$ for some points on the lower branch (N1-5), but this is no longer true for the points around the conjunction point, N1-4, see figure 4.

The temporal evolutions of the complete energy budgets for the operating points are shown in figure 5. On the upper branch of the mode-1 curve, $P_1(F)$ leads in phase, and is closely followed by $\mathrm{d}\bar{E}$ and P_3. The dissipation rate D follows slightly later, since the strength of the thin boundary layer only reaches its peak after the flow is sloshed forward. These are opposed by $\mathrm{d}U_\lambda$ and $\mathrm{d}U_\kappa$, the rate of strain energies of the beam. On the lower branch, the wall deforms more significantly during the oscillations (see figure 5, N1-5). D now leads the phase, and is followed by P_3 and P_1, with $\mathrm{d}E$ slightly behind. The flow structure becomes more complex with flow separations and eddies downstream (see figure 6 below). It is interesting to note that around the turning point (N1-3), all rates of energies are in phase, and the magnitudes (oscillation strength) are much smaller than those of other neutral points. This is presumably because the system is subdued by competing driving mechanisms.

The corresponding pressure, streamline and vorticity contours are shown in figure 6 for points N1-3 and N1-5 on the upper and lower branches. Figure 6 shows that the upper branch solution has smaller wall deformation; therefore a thinner boundary layer. Closer to the turning point N1-3, the boundary layer becomes thicker. The vorticity, which is closely linked to energy dissipation, is not only concentrated near the walls, but also around the narrowest part of the channel. On the lower branch, the viscous boundary layer continues to increase around the narrowest point, and extends to the vicinities of both walls downstream of the collapsible wall. At N1-5, vorticity is almost four times as great compared to N1-3, enhanced by flow separation which increases the energy dissipation further. This indicates that the energy is re-distributed across the channel. The energy change from the upper to lower neutral branches is clearly associated with the deformation of the wall, and the Bernoulli mechanism observed by Luo *et al.* (2008) could well be involved in the self-excited oscillations in the lower-tension region.

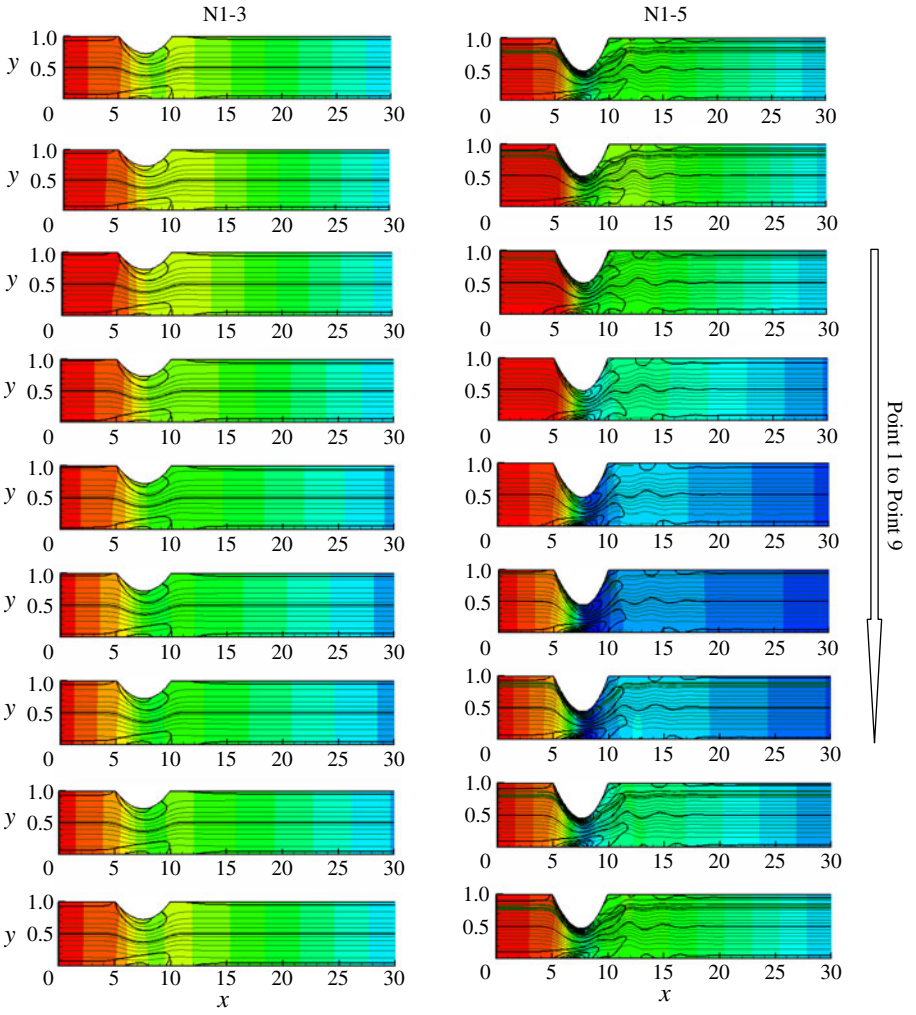

FIGURE 6. (Colour online) Contour plots for N1-3 and N1-5. The streamline contours (thinner) are plotted from 0.02 to 0.36 for N1-3, and 0 to 0.417 for N1-5. The vorticity contours (thicker) are plotted between -4 to 4 for N1-3, and -16 to 14 for N1-5. The pressure contours are indicated by grey scales, which are plotted from 0.05 to 0.65 for N1-3, and 0.05 to 0.95 for N1-5. The time instants 1–9 are marked on figure 5.

4. Discussion

4.1. *Fluid–beam versus fluid–membrane models*

As all simulations are carried out using the fluid–beam model, we now compare the differences of the energy budgets between the fluid–beam and fluid–membrane models when c_λ is very small (=1), $c_\kappa \equiv 0$. Very similar energy budgets are observed for the two models. There are only two differences observed. Firstly, the fluid–beam model predicts a slightly greater growth rate than that of the fluid–membrane one. This is understandable as the fluid–beam model includes wall extension as well as bending stiffness (even though c_λ is small). Secondly, there is very small shape difference in the F–D phase plot. However, the phase direction and all other qualitative features are essentially the same.

While these results may suggest that the fluid–membrane model may be effectively used to model a thin-walled collapsible channel, the major impact of using a fluid–beam model will be for thick-walled channel flows, where the bending effects are greater. However, this aspect is not addressed in the present work.

4.2. *Sign of* $\bar{F}$

Table 2 shows that $\bar{F}$ is definitely positive for three of the mode-1 neutral points selected (N1-1–N1-3), i.e. the influx upstream provides energy into the system to maintain the oscillation. This agrees with the prediction by Jensen & Heil (2003). However, due to limited numerical accuracy, $\mathrm{d}\bar{E}$ is not sufficiently small for N1-4 and N1-5; therefore we cannot be certain that $\bar{F}$ for N1-4 and N1-5 is also definitely positive.

In other words, the mechanism predicted by the asymptotic analysis is no longer valid for the lower branch of the mode-1 neutral curve. This agrees with the recent work by Stewart *et al.* (2010).

4.3. *Energy budget in the flow-driven system*

As we have seen, in the pressure-driven system, the mode-2 neutral curve was completely wrapped by that of mode-1, so mode-2-only states does not occur (and could not be analysed), and the budget analysis concerned mode-1. This suggests that the pressure-driven system is much more unstable compared to the flow-driven system, and offers a much richer dynamic behaviour. A similar observation has been made by previous researchers (Stewart *et al.* 2010). Unlike the flow-driven system, it loses stability to a mode-1 perturbation first when wall stiffness is reduced.

We now compare the energy budget at the threshold of instability with that of the flow-driven system that our group studied previously. In the latter, mode-1 is stable, so the budgets concerns mode-2. Two operating points are chosen on the mode-2 neutral curve by Luo *et al.* (2008), see figure 7. The time-averaged energy quantities for the operating points are listed in table 4.

It is clear that values of $|D_s/\bar{F}|$ computed for these points are no longer two-thirds, even for the upper branch of the neutral curve. In fact, $\bar{F}$ seems to be negative (though closer to zero for N2-lower), showing that the oscillatory energy is extracted by the mean flow from the structure. The inlet pressure is the only driving force to maintain the vibration.

The phase plots of F, P_1 and D in figure 8 show that in the mode-2 neutral oscillation, the phase of F is always ahead of that of D, that is, the F–D relation is clockwise. In addition, no direction change is observed between the F–D phase plots of the upper and lower branches of the mode-2 neutral curve, unlike for the mode-1 curve. Most interestingly, there is a greater phase difference between P_1 and F, especially on the lower branch. This may be due to the absence of the sloshing pattern commonly taking place in mode-1 oscillations, and thus a stronger correlation between P_1 and F. In addition, the constant inlet flow rate also has a significant effect since the phase of F is now only determined by the kinetic energy outflux at the channel outlet.

Comparing with the energy budgets of mode-1 oscillations in the pressure-driven system, one of the significant features of the mode-2 oscillation in the flow-driven system is that the strain energies of the beam have much smaller oscillating amplitudes. The dominant oscillating energy is now $\mathrm{d}E$, which is always in phase with the driving rate of work P_1. If we look at the corresponding flow fields in figure 9, we can see that there is no significant difference in the flow field for the points (N2-upper)

Point	$\bar{F}$	$\bar{P}_1$	$\bar{D}$	$\bar{D}_s$	$\lvert\bar{D}_s/\bar{F}\rvert$	$\mathrm{d}\bar{E}$	ω_i	Re
N2-upper	-5.220×10^{-4}	1.387	1.386	8.338×10^{-5}	0.159	5.924×10^{-6}	2.187	400.0
N2-lower	-1.756×10^{-4}	2.312	2.313	5.152×10^{-3}	28.330	-1.996×10^{-4}	1.299	279.6

TABLE 4. The time-averaged energy quantities at the operating points shown in figure 7, for the flow-driven system.

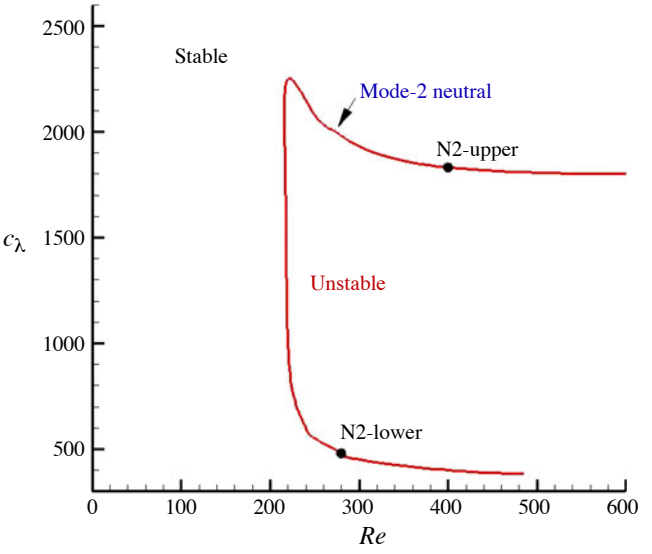

FIGURE 7. (Colour online) The mode-2 neutral curve computed in a similar manner for the flow-driven system (taken from Luo *et al.* 2008), with two operating points. Note that the elastic wall deflection is greater at N2-lower and that the elastic wall deformation is greater at N2-lower than at N2-upper.

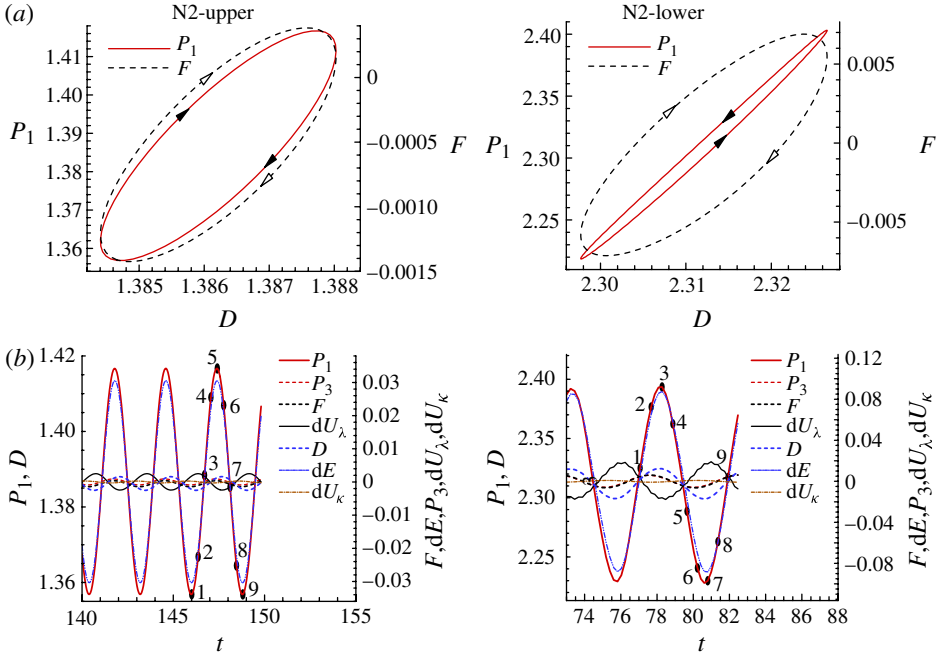

FIGURE 8. (Colour online) (*a*) Phase plots for energies of points N2-upper and N2-lower shown in figure 7, and (*b*) the complete energy budget of these two points plotted against time.

on the upper branch to that of the lower branch (N2-lower), except that for the lower branch, the elastic wall is more severely deformed.

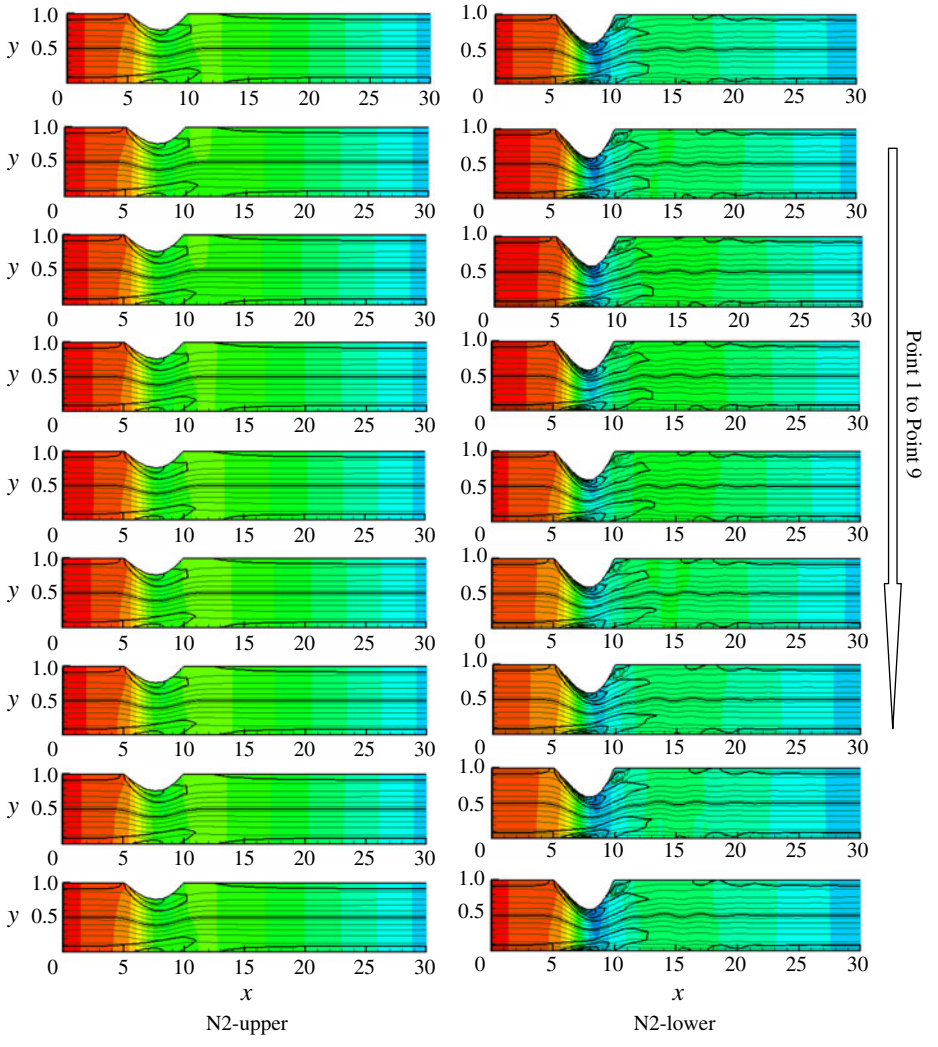

FIGURE 9. (Colour online) Contour plots for the two mode-2 operating points shown in figure 8. The streamline contours (thinner) are plotted from 0.05 to 0.95 for N2-upper and 0.005 to 1.008 for N2-lower. The vorticity contours (thicker) are plotted between −10 to 10 for N2-upper and −25 to 25 for N2-lower. The pressure contours are indicated by grey scales, which are plotted between 0.1 to 1.7 for N2-upper and 0 to 2.25 for N2-lower. The time instants 1–9 are marked on figure 8(*b*).

4.4. *Limitations*

Although an interesting stability structure has been identified in this paper, this has only been investigated for limited parameter regimes. One particular limitation is that throughout the computations, we only studied the case $L = 5$. Therefore, it is not clear how robust the findings are for a system with different length ratios. There are two reasons for this choice. The first one is the computational costs. For each neutral point, we need to perform a sequence of unsteady numerical simulations using bisection methods and scan through the whole (c_λ, Re) space, which is an extremely lengthy process. The second reason for fixing the length is that we believe that the

effective impact of changing the length of the channel is similar to varying the tension (hence c_λ), since one-dimensional models show that length can be scaled out as being proportional to the square of tension (Luo & Pedley 1995). Having said this, the one- and two-dimensional systems may not be analogous in terms of stability structure. There are also other important parameters that could affect the stability structure, such as the external pressure and wall thickness. However, given the expensive nature of the numerical approaches used here, such parameter studies must await alternative models, which are faster and more efficient.

5. Conclusion

In this study, we examine the linear stability and the energy budget of collapsible channel flows with particular focus on the difference between the pressure-driven (inlet pressure specified) and flow-driven (inlet flow specified) systems. It is found that these two systems can produce significantly different stability behaviour. The most notable difference is the existence of the mode-1 oscillation in the pressure-driven system which is absent in the flow-driven system. In addition, the stability structure in the pressure-driven system is no longer a cascade as in the flow-driven case. Instead, mode-1 is the dominant unstable mode in the pressure-driven system, and the mode-2 neutral curve is embraced by the mode-1 neutral curve. In other words, it is not possible for the system to have purely mode-2 oscillations in the parameter space studied.

Detailed energy budget analysis at the neutral points reveals that the mechanism responsible for the small deformation oscillation in the pressure-driven system may be the same as suggested by Jensen & Heil (2003). Namely, on the upper branch of mode-1 when the wall stiffness (or tension) is high, there appears to be a ratio close to $2/3$ between the averaged flow influx and the energy dissipation associated with the oscillations. However, on the lower branch of the mode-1 neutral curve, greater wall deformation induces stronger energy dissipation towards the centre of the tube, especially around the narrowest section. This changes the energy balance, and the two-thirds ratio between the influx and oscillatory dissipation no longer holds. The same conclusion was reached independently by Stewart *et al.* (2010). There is a distinct change in the phase plot of the work done by upstream pressure (or the net kinetic energy influx) and the rate of viscous dissipation: on the upper branch of the mode-1 neutral curve, the direction of the phase plot is clockwise; on the lower branch, it is anticlockwise. However, at the turning point, they are virtually in phase. It is possible that the Bernoulli effects may be operating together with the Stokes layer mechanism on the lower branch. For comparison, we also present the energy budget for the mode-2 neutral curve of the flow-driven system. One important finding is that the averaged flow influx is likely to be positive for mode-1 neutral points of the pressure-driven system (though a couple of the influx values we computed are too small to be clearly positive), which again agrees with the one-dimensional asymptotic predication by Stewart *et al.* (2009). However, it is negative for all the mode-2 neutral points of the flow-driven system.

The first author is funded by a Dorothy Hodgkin's Postgraduate Award at the University of Glasgow, UK. This work is in part supported by the EPSRC grant (No. EP/G015651) and the Royal Society UK–China Joint Project (No. 2005/R4-JP). Special thanks to Professors O. E. Jensen and T. J. Pedley for useful discussions and suggestions for this work.

Appendix. Proof of the geometrical conservation law (GCL) of the numerical scheme

We now show that our numerical scheme satisfies the GCL condition. For a movable mesh, GCL requires that:

$$\frac{\partial}{\partial t}\int_V \mathrm{d}V = \int_S D\cdot v\,\mathrm{d}S, \tag{A 1}$$

where D is the velocity of the mesh. In our finite element scheme, we use 6-node triangle elements with straight sides (1-4-2, 2-5-3, and 5-6-1). For each element, we have

$$\begin{aligned}\frac{\partial}{\partial t}\int_V \mathrm{d}V &= \frac{\partial}{\partial t}[(x_1-x_3)(y_2-y_3)-(x_2-x_3)(y_1-y_3)]/2\\ &= [(u_1-u_3)(y_2-y_3)+(x_1-x_3)(v_2-v_3)\\ &\quad -(u_2-u_3)(y_1-y_3)-(x_2-x_3)(v_1-v_3)]/2.\end{aligned} \tag{A 2}$$

We then use the spine method and always define the node 4 to be at the centre of the side (1-4-2), the velocity of this side is then a linear function of l, namely it can be written as

$$D = D_1(1-l/L)+D_2 l/L, \tag{A 3}$$

where L is the length of side 1-4-2, $D_i = u_i e_x + v_i e_y$ is the mesh velocity at node i. The normal of side (1-4-2) can be written as

$$v = [(y_2-y_1)e_x-(x_2-x_1)e_y]/L. \tag{A 4}$$

Similarly for the other two sides. Substituting (A 3) and (A 4) into the right-hand side of (A 1) we have

$$\begin{aligned}\int_S D\cdot v\,\mathrm{d}S &= [(u_1+u_2)(y_2-y_1)-(v_1+v_2)(x_2-x_1)]/2\\ &\quad +[(u_2+u_3)(y_3-y_2)-(v_2+v_3)(x_3-x_2)]/2\\ &\quad +[(u_3+u_1)(y_1-y_3)-(v_3+v_1)(x_1-x_3)]/2.\end{aligned} \tag{A 5}$$

By comparing (A 2) and (A 5), and note that x_i, y_i, u_i, v_i are all nodal unknowns (no errors induced by the discretization), it is easy to confirm that (A 1) is exactly satisfied.

REFERENCES

BERTRAM, C. D. 1982 2 modes of instability in a thick-walled collapsible tube conveying a flow. *J. Biomech.* **15** (3), 223–224.

BERTRAM, C. D. & ELLIOTT, N. S. J. 2003 Flow-rate limitation in a uniform thin-walled collapsible tube, with comparison to a uniform thick-walled tube and a tube of tapering thickness. *J. Fluids Struct.* **17** (4), 541–559.

BERTRAM, C. D. & PEDLEY, T. J. 1982 A mathematical-model of unsteady collapsible tube behavior. *J. Biomech.* **15** (1), 39–50.

BERTRAM, C. D., RAYMOND, C. J. & PEDLEY, T. J. 1990 Mapping of instabilities for flow through collapsed tubes of differing length. *J. Fluids Struct.* **4** (2), 125–153.

CAI, Z. X. & LUO, X. Y. 2003 A fluid–beam model for flow in collapsible channels. *J. Fluids Struct.* **17**, 123–144.

CANCELLI, C. & PEDLEY, T. J. 1985 A separated-flow model for collapsible-tube oscillations. *J. Fluid Mech.* **157**, 375–404.

CONRAD, W. A. 1969 Pressure-flow relationships in collapsible tubes. *IEEE Trans. Biomed. Engng* **16** (4), 284–295.

ÉTIENNE, S., GARON, A. & PELLETIER, D. 2009 Perspective on the geometric conservation law and finite element methods for ALE simulations of incompressible flow. *J. Comput. Phys.* **228** (7), 2313–2333.

GARBOW, B. S. 1978 The QZ algorithm to solve the generalized eigenvalue problem for complex matrices. *ACM Trans. Math. Softw.* **4** (4), 404–410.

HAZEL, A. L. & HEIL, M. 2003 Steady finite-Reynolds-number flows in three-dimensional collapsible tubes. *J. Fluid Mech.* **486**, 79–103.

HEIL, M. & WATERS, S. L. 2008 How rapidly oscillating collapsible tubes extract energy from a viscous mean flow. *J. Fluid Mech.* **601**, 199–227.

ISHIZAKA, K. 1972 Synthesis of voiced sounds from a two-mass model of the vocal cords. *Bell Syst. Tech. J.* **51**, 1233–1268.

JENSEN, O. E. 1990 Instabilities of flow in a collapsed tube. *J. Fluid Mech.* **220**, 623–659.

JENSEN, O. E. & HEIL, M. 2003 High-frequency self-excited oscillations in a collapsible-channel flow. *J. Fluid Mech.* **481**, 235–268.

KAMM, R. D. & SHAPIRO, A. H. 1979 Unsteady flow in a collapsible tube subjected to external pressure or body forces. *J. Fluid Mech.* **95** (1), 1–78.

KATZ, A. I., CHEN, Y. & MORENO, A. H. 1969 Flow through a collapsible tube: experimental analysis and mathematical model. *Biophys. J.* **9** (10), 1261–1279.

LIU, H. F., LUO, X. Y., CAI, Z. X. & PEDLEY, T. J. 2009 Sensitivity of unsteady collapsible channel flows to modelling assumptions. *Commun. Numer. Meth. Engng* **25** (5), 483–504.

LUO, X. Y., CAI, Z. X., LI, W. G. & PEDLEY, T. J. 2008 The cascade structure of linear instability in collapsible channel flows. *J. Fluid Mech.* **600**, 45–76.

LUO, X. Y. & PEDLEY, T. J. 1995 A numerical simulation of steady flow in a 2-D collapsible channel. *J. Fluids Struct.* **9** (2), 149–174.

LUO, X. Y. & PEDLEY, T. J. 1996 A numerical simulation of unsteady flow in a two-dimensional collapsible channel. *J. Fluid Mech.* **314**, 191–225.

LUO, X. Y. & PEDLEY, T. J. 1998 The effects of wall inertia on flow in a two-dimensional collapsible channel. *J. Fluid Mech.* **363**, 253–280.

LUO, X. Y. & PEDLEY, T. J. 2000 Multiple solutions and flow limitation in collapsible channel flows. *J. Fluid Mech.* **420**, 301–324.

MARZO, A., LUO, X. Y. & BERTRAM, C. D. 2005 Three-dimensional collapse and steady flow in thick-walled flexible tubes. *J. Fluids Struct.* **20** (6), 817–835.

PEDLEY, T. J. & LUO, X. Y. 1998 Modelling flow and oscillations in collapsible tubes. *Theor. Comput. Fluid Dyn.* **10** (1), 277–294.

SHAPIRO, A. H. 1977 Steady flow in collapsible tubes. *J. Biomech. Engng* **99**, 126.

STEWART, P. S., HEIL, M., WATERS, S. L. & JENSEN, O. E. 2010 Sloshing and slamming oscillations in collapsible channel flow. *J. Fluid Mech.* **662**, 288–319.

STEWART, P. S., WATERS, S. L. & JENSEN, O. E. 2009 Local and global instabilities of flow in a flexible-walled channel. *Eur. J. Mech.* B/*Fluids* **28** (4), 541–557.

WHITTAKER, R. J., HEIL, M., BOYLE, J., JENSEN, O. E. & WATERS, S. L. 2010*a* The energetics of flow through a rapidly oscillating tube. Part 2. Application to an elliptical tube. *J. Fluid Mech.* **648**, 123–153.

WHITTAKER, R. J., HEIL, M., JENSEN, O. E. & WATERS, S. L. 2010*b* A rational derivation of a tube law from shell theory. *Q. J. Mech. Appl. Maths* **63** (4), 465.

WHITTAKER, R. J., HEIL, M., JENSEN, O. E. & WATERS, S. L. 2010*c* Predicting the onset of high-frequency self-excited oscillations in elastic-walled tubes. *Proc. R. Soc. Lond.* A **466**, 3635.

WHITTAKER, R. J., WATERS, S. L., JENSEN, O. E., BOYLE, J. & HEIL, M. 2010*d* The energetics of flow through a rapidly oscillating tube. Part 1. General theory. *J. Fluid Mech.* **648**, 83–121.

ZHU, Y., LUO, X. Y. & OGDEN, R. W. 2008 Asymmetric bifurcations of thick-walled circular cylindrical elastic tubes under axial loading and external pressure. *Intl J. Solids Struct.* **45** (11–12), 3410–3429.

ZHU, Y., LUO, X. Y. & OGDEN, R. W. 2010 Nonlinear axisymmetric deformations of an elastic tube under external pressure. *Eur. J. Mech.* A/*Solids* **29**, 216–229.